International Journal of Solids and Structures 150 (2018) 197–207

Contents lists available at ScienceDirect

International Journal of Solids and Structures

journal homepage: www.elsevier.com/locate/ijsolstr

Stress-point method for stabilizing zero-energy modes in non-ordinary state-based peridynamics

J. Luo [a,*], V. Sundararaghavan [b]

[a] Department of Mechanical Engineering, University of Michigan, Ann Arbor, USA
[b] Department of Aerospace Engineering, University of Michigan, 1320 Beal Avenue, Ann Arbor, MI 48109, USA

ARTICLE INFO

Article history:
Received 2 January 2018
Revised 11 June 2018
Available online 15 June 2018

Keywords:
Zero-energy mode
Peridynamics
State based
Stress points
Particle methods

ABSTRACT

Non-ordinary state–based peridynamics is a promising continuum mechanics theory that combines nonlocal dynamics with conventional material models. Within this theory, the correspondence principle can be invoked to compute deformation gradients from the computed displacement fields. However, correspondence based models are prone to a zero-energy mode. This paper proposes the use of stress points to resolve this issue in the peridynamic family with nearest-neighbor discretizations. Each particle horizon is assigned with stress points at which derivatives of field variables are computed. The method is first demonstrated in a simple 1D problem and is compared with the analytical solution and other control methods. 2D and 3D examples are compared with the finite-element method. Zero-energy modes are shown to be completely damped in all cases. The computation efficiency of the explicit stress-point based peridynamic model is analyzed in the end.

1. Introduction

In classical elasticity, stress at a point is locally dependent on the strain at that point which leads to stress singularities at crack tips and dislocation cores. To resolve this issue, generalized continuum theories have been developed that introduce a length-scale via the assumption of non-locality (Bažant et al., 1984; Ghosh et al., 2013; 2014; Sundararaghavan and Waas, 2011; Coleman and Hodgdon, 1985). In these theories, length scale dependent constitutive laws that involve higher-order strain or stress gradients and higher order stiffness tensors are introduced. Peridynamics, introduced as an alternative integral formulation for continuum mechanics (Silling, 2000), is a relatively new theory that naturally lends itself to the use of meshfree and particle-based discretizations. In the particle-based peridynamic approach, the motion of material points is modeled by an integral operator that sums internal forces between particles in this horizon similar to a molecular dynamics approach. However, the original bond–based peridynamic model which assumes pairwise forces between particles resulted in a fixed Poisson's ratio of 0.25. A generalized Non-Ordinary State-Based (NOSB) peridynamics theory was later proposed by Silling et al. (2007), in which particles interact with force states that may be computed from conventional constitutive models. Thus, the nonlocality is conveniently introduced without the need to alter the underlying constitutive equations. The deformation measure in this model is computed by integrating motion of particles across a finite horizon via the correspondence principle. Using this approach, the method can directly model sharp displacement singularities and discontinuities (Sun and Sundararaghavan, 2014; Agwai et al., 2011; Madenci and Oterkus, 2014; Gerstle, 2015).

One particular drawback of NOSB peridynamics using correspondence material models is the presence of zero-energy modes, which is described in detail in several recent references (Silling, 2017; Breitenfeld et al., 2014; Tupek and Radovitzky, 2014; Yaghoobi and Chorzepa, 2017). For example, in 1D problems with nearest neighbor interactions, the correspondence principle relates three displacements to one deformation gradient. This results in a null space where some deformations do not play a role in the computed gradient. Recent papers have attempted to resolve the instability numerically by adding fictitious springs between particles and hourglass force terms (Breitenfeld et al., 2014; Littlewood, 2011). However, these methods have failed to completely remove the instability and, in addition, employed coefficients or formulations that are sensitive to the mesh size and chosen on a case-by-case basis. Another branch of methods modifies the influence functions, either to provide an average-weighted displacement (Wu and Ben, 2015) or to use higher-order approximations to solve nonlocal peridynamic equations(Madenci et al., 2016; Yaghoobi and Chorzepa, 2017). These methods are effective in increasing the ac-

* Corresponding author.
E-mail addresses: jiangyi@umich.edu (J. Luo), veeras@umich.edu (V. Sundararaghavan).

https://doi.org/10.1016/j.ijsolstr.2018.06.015
0020-7683/

curacy with enlarged horizons, nevertheless, zero-energy modes still remain in the deformation gradient due to the absence of the center particle. Recently Silling (2017) has provided a careful examination of zero-energy modes in the context of a material model instability.

In the current work, we propose the stress-point approach, as a numerical means to mitigate zero-energy modes with nearest-particle-horizon discretizations. The use of stress points has been proposed in the past for other integral methods such as smoothed particle hydrodynamics to address tensile instability issues (Dyka et al., 1997; Vignjevi et al., 2000). The idea is straightforward. Addition of even one more independent stress point in 1D problems leads to two gradients and three displacements which significantly reduces the null space. This stress-point peridynamic model is first demonstrated in a simple 1D problem and then applied to higher-dimensional problems. Using these numerical examples, we show that zero-energy-mode oscillations in all solutions are completely damped. Beyond zero-energy modes, the error in the stresses due to the affine mapping enforced in the correspondence formula is improved as well.

This paper will start Section 2 with a review of the NOSB peridynamics theory. Brief explanations on the origin of zero-energy modes and previous solutions by using supplementary particle forces are followed. The numerical stress-point peridynamic approach is then proposed in Section 3. Section 4 introduces an adaptive dynamic relaxation algorithm. This dynamic solver has been demonstrated effective and efficient in solving peridynamic equations (Luo et al., 2017). Numerical examples are shown and discussed in Section 5. In the 1D example, the stress-point results are compared with the analytical solution and other control methods with artificial force terms. The effect of zero-energy modes in higher-dimensional stress-point solutions are calculated and analyzed with a reference of smooth finite-element method results. A numerical efficiency test of the stress-point model is conducted based on different dimensional examples before the final section where conclusions and future work are discussed.

2. Peridynamic model and zero-energy modes

2.1. Non-ordinary state-based peridynamics

NOSB peridynamics is first presented by Silling et al. (2007) in 2007, which is a nonlocal integral reformulation of the continuum theory. Consider a material point $\mathbf{x}$ in the reference configuration which can only interact with its neighboring points $\mathbf{x}'$ in a self-center horizon $\mathcal{H}_{\mathbf{x}}$ with a finite radius δ. Given a displacement field $\mathbf{u}$, the current configuration is then represented by $\mathbf{y}=\mathbf{x}+\mathbf{u}$. Let the initial physical domain be $\mathcal{B}_0$ at time $t=0$ while $\mathcal{B}_1$ is the deformed domain (shown in Fig. 1).

With the introduction of the deformation vector state $\underline{\mathbf{Y}}=\underline{\mathbf{Y}}[\mathbf{x},t]\langle\mathbf{x}'-\mathbf{x}\rangle=\mathbf{y}'-\mathbf{y}$, which denotes the deformed state of the bond $\boldsymbol{\xi}=\mathbf{x}'-\mathbf{x}$, the deformation gradient $\mathbf{F}$ at particle $\mathbf{x}$ is reformulated as a nonlocal integration over the horizon:

$$\mathbf{F}=\left(\int_{\mathcal{H}_{\mathbf{x}}}\omega(\underline{\mathbf{Y}}\otimes\boldsymbol{\xi})dV_{\mathbf{x}'}\right)\mathbf{K}^{-1}, \tag{1}$$

where ω is an influence function defined at particle $\mathbf{x}$ in $\mathcal{H}_{\mathbf{x}}$. It weights the influence of each neighbor $\mathbf{x}'$ on the particle $\mathbf{x}$ and can be selected as a spherical function based on the initial bond length, i.e., $\omega=\omega(|\boldsymbol{\xi}|)$. $\mathbf{K}$ is a symmetric shape tensor at particle $\mathbf{x}$, defined as

$$\mathbf{K}=\int_{\mathcal{H}_{\mathbf{x}}}\omega(\boldsymbol{\xi}\otimes\boldsymbol{\xi})dV_{\mathbf{x}'}. \tag{2}$$

Finally, the equation of motion of state-based peridynamics at time t is

$$\rho\ddot{\mathbf{u}}(\mathbf{x},t)=\mathbf{L}(\mathbf{x},t)+\mathbf{b}(\mathbf{x},t),$$

$$\mathbf{L}(\mathbf{x},t)=\int_{\mathcal{H}}\{\underline{\mathbf{T}}[\mathbf{x},t]\langle\mathbf{x}'-\mathbf{x}\rangle-\underline{\mathbf{T}}[\mathbf{x}',t]\langle\mathbf{x}-\mathbf{x}'\rangle\}dV_{\mathbf{x}'}, \tag{3}$$

where $\underline{\mathbf{T}}[\mathbf{x},t]\langle\mathbf{x}'-\mathbf{x}\rangle$ is the force vector state operating on the bond $\boldsymbol{\xi}=\mathbf{x}'-\mathbf{x}$ at particle $\mathbf{x}$ at time t and $\mathbf{b}(\mathbf{x},t)$ is the body force density. In connection to the classical continuum theory, the force state $\underline{\mathbf{T}}$ can be obtained from the first Piola–Kirchhoff stress, $\mathbf{P}$, at particle $\mathbf{x}$ as follows (Silling et al., 2007):

$$\underline{\mathbf{T}}[\mathbf{x},t]\langle\mathbf{x}'-\mathbf{x}\rangle=\omega\mathbf{P}\mathbf{K}^{-1}\boldsymbol{\xi}, \tag{4}$$

where $\mathbf{P}$ could be found from a classical stress-strain constitutive model using kinematics derived from the deformation gradient $\mathbf{F}$. This NOSB peridynamic correspondence material model will be applied in the following examples in this paper.

2.2. Zero-energy modes and control methods with supplementary particle forces

This inherent stability issue is a result of weak couplings between particles (Breitenfeld et al., 2014; Tupek and Radovitzky, 2014; Wu and Ben, 2015; Yaghoobi and Chorzepa, 2017). A simple example is discussed below to help understanding its origin.

Consider a 2D regular lattice shown in Fig. 2. The deformation gradient at the beginning is calculated as $\mathbf{F}_{\text{old}}$. After a small displacement disturbance $\mathbf{u}_{\text{d}}$ is given at the center particle $\mathbf{x}$, the new deformation gradient $\mathbf{F}_{\text{new}}$ is then calculated based on (1) as

$$\begin{aligned}\mathbf{F}_{\text{new}}&=\left(\int_{\mathcal{H}_{\mathbf{x}}}\omega(\underline{\mathbf{Y}}_{\text{new}}\otimes\boldsymbol{\xi})dV_{\mathbf{x}'}\right)\mathbf{K}^{-1}\\&=\left(\int_{\mathcal{H}_{\mathbf{x}}}\omega\left[(\underline{\mathbf{Y}}_{\text{old}}-\mathbf{u}_{\text{d}})\otimes\boldsymbol{\xi}\right]dV_{\mathbf{x}'}\right)\mathbf{K}^{-1}\\&=\mathbf{F}_{\text{old}}-\mathbf{u}_{\text{d}}\otimes\left(\int_{\mathcal{H}_{\mathbf{x}}}\omega\boldsymbol{\xi}dV_{\mathbf{x}'}\right)\mathbf{K}^{-1}.\end{aligned} \tag{5}$$

With the assumption of a regular lattice mesh and a spherically symmetric influence function ω, the integration term on the right hand side will vanish. The missing role of the center particle is one of the causes of zero-energy modes, or hourglass modes, which is a common stability issue in mesh-free methods, FEM, and numerical schemes with central difference discretization (Bower, 2009; Gerstle, 2015; LeVeque, 2007; Flanagan and Belytschko, 1981).

Some previous ideas to address this issue include introduction of artificial force state, $\underline{\mathbf{T}}_{\text{a}}[\mathbf{x}]\langle\mathbf{x}'-\mathbf{x}\rangle$, at particle $\mathbf{x}$ on the bond $\mathbf{x}'-\mathbf{x}$, which is

$$\underline{\mathbf{T}}[\mathbf{x},t]\langle\mathbf{x}'-\mathbf{x}\rangle=\omega\mathbf{P}\mathbf{K}^{-1}\boldsymbol{\xi}+\underline{\mathbf{T}}_{\text{a}}[\mathbf{x}]\langle\mathbf{x}'-\mathbf{x}\rangle. \tag{6}$$

This artificial force can be generated by either interconnected springs or average displacement states (Breitenfeld et al., 2014). Linear springs are introduced between particles in the first method:

$$\underline{\mathbf{T}}_{\text{a}}[\mathbf{x}]\langle\mathbf{x}'-\mathbf{x}\rangle=C_1\omega[\mathbf{u}(\mathbf{x}')-\mathbf{u}(\mathbf{x})], \tag{7}$$

where C_1 is a spring constant. The second method computes the added force based on an average of all displacement states over one horizon, which is

$$\underline{\mathbf{T}}_{\text{a}}[\mathbf{x}]\langle\mathbf{x}'-\mathbf{x}\rangle=C_2\int_{\mathcal{H}_{\mathbf{x}}}\omega[\mathbf{u}(\mathbf{x}')-\mathbf{u}(\mathbf{x})]dV_{\mathbf{x}'}. \tag{8}$$

These supplementary forces have a suppression effect on zero-energy modes. However, this effect highly depends on the mesh size and the problem itself. In addition, to determine the optimum values of the artificial coefficients, i.e., C_1 and C_2, calculations need to be performed beforehand (Breitenfeld et al., 2014; Yaghoobi and Chorzepa, 2017). None of these methods completely suppresses zero energy modes. The stress-point approach is presented next.

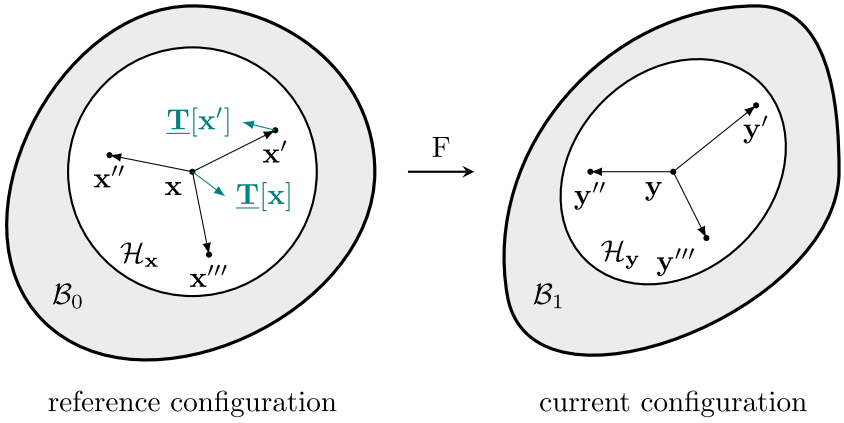

Fig. 1. Kinematics of peridynamics: Particle **x** is bonded to all particles (**x**′, **x**″, and **x**‴) within a region $\mathcal{H}_{\mathbf{x}}$. After deformation, particle **x** maps to particle **y** and the process can be described by an averaged deformation gradient **F**. $\underline{\mathbf{T}}[\mathbf{x}, t]\langle \mathbf{x}' - \mathbf{x}\rangle$ and $\underline{\mathbf{T}}[\mathbf{x}', t]\langle \mathbf{x} - \mathbf{x}'\rangle$ are force vector states in the reference configuration at particle **x** and **x**′, respectively. The notation of these two force states are shorten as $\underline{\mathbf{T}}[\mathbf{x}]$ and $\underline{\mathbf{T}}[\mathbf{x}']$ in this figure only for the sake of brevity. In the NOSB peridynamics theory, these two force vector states are not necessarily parallel and can be obtained from the classical stress tensor.

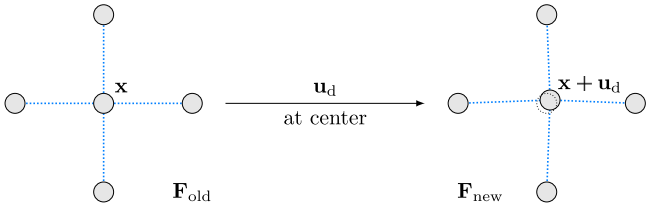

Fig. 2. An illustration of zero-energy modes in a 2D regular lattice. Small disturbance is given at the center particle, which, however, has no impact on calculating the deformation gradient.

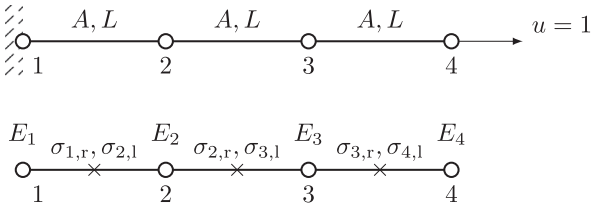

Fig. 3. An illustration of the stress-point peridynamic scheme on a 1D elastic bar. The bar is fixed at left with a displacement loading at right and discretized into four peridynamic particles. The total length and cross-sectional area are 3*L* and *A*, respectively. Assume particles only interact with nearest neighbors.

3. Stress-point approach for NOSB peridynamics with a correspondence material model

3.1. 1D stress-point peridynamic scheme

Based on the stress-point approach addressing tension instability in smoothed-particle hydrodynamics methods (Dyka et al., 1997), and its relevance to particle-based model of peridynamics (Ganzenmüller et al., 2015), a new stress-point scheme is proposed and explained below. In order to enhance particle connections, a few quantities related to stress are calculated twice in the horizon of particles. Take the 1D bar in Fig. 3 as an example. Two stresses, σ_{l} and σ_{r}, are calculated at left and right of each particle by splitting the neighborhood and using the corresponding bond, respectively. For instance, $\sigma_{2,\,\mathrm{l}}$ and $\sigma_{2,\,\mathrm{r}}$ are calculated on the two sides of particle 2 while only $\sigma_{1,\,\mathrm{r}}$ is calculated at the right side of particle 1. Overall, the shape tensor, deformation gradient, strain, and stress are computed at stress points located at the middle of adjacent particles, in contrast with field variables such as displacement and material properties which are calculated at particles.

Note that, even at the same location, $\sigma_{1,\,\mathrm{r}}$ is not always equal to $\sigma_{2,\,\mathrm{l}}$. They are distributed in the horizons of particle 1 and 2, respectively. Quantities are visible only in a shared horizon to protect the completeness and closure of horizons.

Take particle 2 for example and assume particles only interact with nearest neighbors. Deformation gradients $F_{2,\,\mathrm{l}}$ and $F_{2,\,\mathrm{r}}$ only consider the corresponding bond on the left and right of particle 2, respectively (using Eq. (1), and $\omega = 1$):

$$F_{2,\mathrm{l}} = [-(u_1 - u_2 - L)]AL^2/K_{2,\mathrm{l}} = \frac{u_2 - u_1}{L} + 1,$$
$$F_{2,\mathrm{r}} = (u_3 - u_2 + L)AL^2/K_{2,\mathrm{r}} = \frac{u_3 - u_2}{L} + 1, \tag{9}$$

where the shape tensors $K_{2,\,\mathrm{l}}$ and $K_{2,\,\mathrm{r}}$ are calculated as

$$K_{2,\mathrm{l}} = (-L)(-L)AL = AL^3,$$
$$K_{2,\mathrm{r}} = L \cdot L \cdot AL = AL^3. \tag{10}$$

As for the equation of motion at particle 2, it turns into

$$(-\sigma_{1,\mathrm{r}}K_{1,\mathrm{r}}^{-1}L - \sigma_{2,\mathrm{l}}K_{2,\mathrm{l}}^{-1}L)V + (\sigma_{2,\mathrm{r}}K_{2,\mathrm{r}}^{-1}L + \sigma_{3,\mathrm{l}}K_{3,\mathrm{l}}^{-1}L)V = 0$$
$$\Longrightarrow -\sigma_{1,\mathrm{r}} - \sigma_{2,\mathrm{l}} + \sigma_{2,\mathrm{r}} + \sigma_{3,\mathrm{l}} = 0. \tag{11}$$

If we make a further step to assume the material is elastic with a constant Young's modulus *E* and under small deformation (see Appendix A.2), Eq. (11) then becomes

$$u_1 - 2u_2 + u_3 = 0. \tag{12}$$

Compared to the original peridynamic scheme (Appendix A.1), the difference is that all particle displacements are involved in (12). This treatment will prevent the zero-energy mode occurring from the source.

3.2. Higher-dimensional stress-point peridynamic schemes

Two guidelines are used when we extend the stress-point approach to higher dimensions. The first is to enhance connections between particles by using all particle displacements in the deformation measures. The second is to keep the completeness and closure of horizons, by modeling stress interactions similar to the 1D scheme.

Assume particles can only interact with nearest neighbors. Starting from 2D problems, a scheme with two stress points is adopted. More stress points can be employed to increase the accuracy, however, higher computation cost is expected. As illustrated

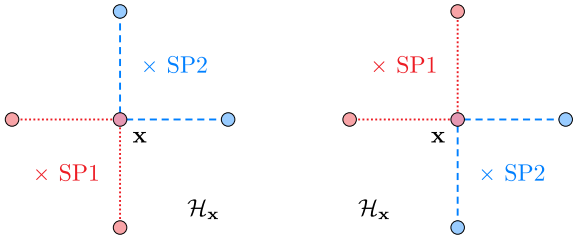

Fig. 4. A 2D scheme with two stress points. Blue and red stress points only take charge of bonds with the same color at the same side. There are two choices based on the location of stress points. (For interpretation of the references to color in this figure legend, the reader is referred to the web version of this article.)

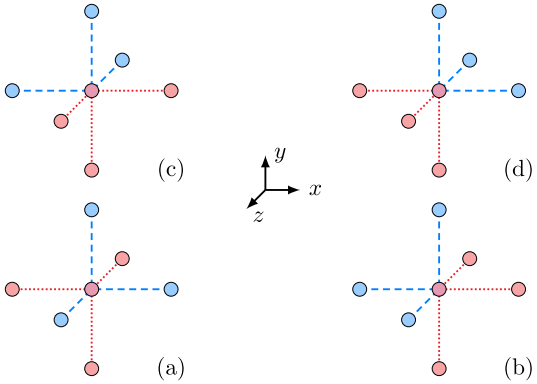

Fig. 5. A 3D scheme with two stress points. Blue and red stress points only take charge of bonds with the same color at the same side. There are four choices (a)–(d) based on the location of stress points. (For interpretation of the references to color in this figure legend, the reader is referred to the web version of this article.)

in Fig. 4, the two stress points are located at two sides of the center particle and each one only takes charge of the two bonds on the same side. For example, blue stress points (SP2) only consider blue bonds and the same with red stress points (SP1). Hence there are two cases in 2D problems.

Similar to the 2D scheme above, only two stress points are employed in our 3D model. However, there are totally four cases in 3D problems, as shown in Fig. 5, and each stress point owns three bonds in the horizon. To avoid directional bias, we randomly select the location of stress-points at each particle in the following 2D and 3D examples, using a random number generator to choose one case from Figs. 4 and 5 when assigning stress points to each particle.

When it comes to the equation of motion, we compute the force states based on stresses sharing the common bond, as we showed (11) in the 1D stress-point model. In other words, the stress term in (4) are calculated at the stress point owing the same bond $\boldsymbol{\xi}$. During postprocessing, the stress is recalculated as the average of stress-point values in one horizon once we find the displacement fields. Another case to consider are the boundary particles because their horizons are defective. We allocate only one stress point to include all the bonds in the boundary particle to solve this problem.

4. Adaptive dynamic relaxation method

In this paper, we use an explicit dynamic relaxation method with the quasi-static assumption previously described in our work in Luo et al. (2017) and not reproduced for brevity. This explicit method introduces an adaptive artificial damping to obtain a steady-state solution with a large number of iterations. Its computation efficiency can be strongly enhanced with an optimum damping coefficient which is determined by Rayleigh's quotient (Kilic and Madenci, 2010). Here we primarily discuss the change in time stepping scheme that is needed when using the method alongside the new stress point approach.

An appropriate time step Δt for the 1D peridynamic model is based on the wave speed c_s using the Courant–Friedrichs–Lewy (CFL) condition (LeVeque, 2007):

$$\Delta t \leq 2\Delta x/c_s, \tag{13}$$

where Δx is the minimal grid size, or the minimal bond length in peridynamics.

In higher-dimensional cases, the CFL condition is more stringent. Assuming that we are dealing with n-dimensional problems using a uniform grid and the wave speeds along different directions are the same, the critical time step size becomes

$$\Delta t \leq \frac{2}{n}\Delta x \cdot \sqrt{\rho/E_{max}}, \tag{14}$$

in which ρ is the density and E_{max} is the maximum component of the elastic stiffness matrix is used to approximate the maximum possible wave speed.

However, the stability condition of the new stress-point model is more restricted and changes to a half of (14):

$$\Delta t \leq \frac{1}{n}\Delta x \cdot \sqrt{\rho/E_{max}}. \tag{15}$$

A detailed derivation of the time step size from a 1D elastic problem is described in Appendix A. Note that the CFL limit condition in (14) could be quite conservative since the derivation is based on just the closest neighbors.

Two absolute errors ε_1 and ε_2 are calculated during iterations with the definitions as

$$\varepsilon_1 = \frac{\|\mathbf{L}(\mathbf{x})\|_2}{N} \text{ and } \varepsilon_2 = \frac{\|\delta\mathbf{u}\|_2}{N}, \tag{16}$$

where l^2-norm is employed and N is the total number of particles. The first error ε_1 describes the degree to which the residual approaches to zero while the second one ε_2 denotes the magnitude of displacement increments between two adjacent iteration steps. In order to normalize the error from initial guesses, two corresponding relative errors e_1 and e_2 are then computed and monitored, which are

$$e_1 = \frac{\varepsilon_1}{\varepsilon_1^0} \text{ and } e_2 = \frac{\varepsilon_2}{\varepsilon_2^0}, \tag{17}$$

where ε^0 is the initial absolute error at the first iteration. Iterations stop only when both criteria, $e_{1,2} < e_l$, are satisfied, where $e_l = 10^{-6}$.

5. Examples and discussions

We assume materials are elastic under small deformation in the following numerical examples. Strain tensor is computed as $\epsilon = 1/2(\mathbf{F}^T + \mathbf{F}) - \mathbf{I}$, where $\mathbf{I}$ is the identity tensor. Cauchy stress $\boldsymbol{\sigma} = \mathbf{D} : \boldsymbol{\epsilon}$, is used in lieu of $\mathbf{P}$ (assuming small deformations) in (4) and $\mathbf{D}$ is an isotropic elastic modulus tensor. The horizon radius δ is kept minimum merely including the nearest neighbor particles and the influential function ω is set to be constant 1 for simplicity.

5.1. 1D bar test

In order to compare with the analytical solution and control methods with adding supplementary particles forces, a similar 1D elastic bar test in Breitenfeld et al. (2014); Yaghoobi and Chorzepa (2017) is conducted, as shown in Fig. 6. The bar with a total length L_{tot} is discretized as n peridynamic particles. Dirichlet

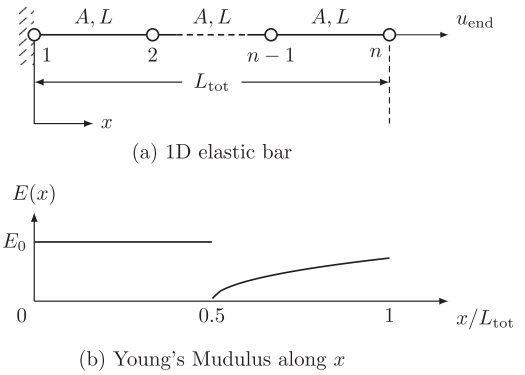

(a) 1D elastic bar

(b) Young's Mudulus along x

Fig. 6. A 1D elastic bar under tension with a Young's modulus varied along the x axis.

boundary conditions, $u_1 = 0$ and $u_n = u_{end}$, are applied on the two sides of the truss. A variable Young's modulus is adopted as

$$E(x) = \begin{cases} E_0 & 0 \le x \le L_{tot}/2 \\ E_0\left(1 + \frac{\beta}{2\alpha}\frac{1}{\sqrt{x/L_{tot} - 1/2}}\right)^{-1} & L_{tot}/2 < x \le L_{tot} \end{cases}, \tag{18}$$

and the analytical displacement $u(x)$ and strain $\epsilon(x)$ solutions are

$$u(x) = \begin{cases} \alpha x & 0 \le x \le L_{tot}/2 \\ \alpha x + \beta L_{tot}\sqrt{x/L_{tot} - 1/2} & L_{tot}/2 < x \le L_{tot} \end{cases}, \tag{19}$$

$$\epsilon(x) = \begin{cases} \alpha & 0 \le x \le L_{tot}/2 \\ \alpha + \beta\left(2\sqrt{x/L_{tot} - 1/2}\right)^{-1} & L_{tot}/2 < x \le L_{tot} \end{cases}, \tag{20}$$

where parameters are selected as $L_{tot} = 1$, $E_0 = 1$, $u_{end} = 0.005$, $\alpha = 0.001$, and $\beta = 0.004\sqrt{2}$. Note that the expression of Young's modulus is slightly different from the references (Breitenfeld et al., 2014; Yaghoobi and Chorzepa, 2017). This is because parameters α and β adopted in this paper are dimensionless.

We define two local amplitudes of oscillation, $a_{u,i}$ and $a_{e,i}$, at particle i to quantitatively measure the effect of zero-energy modes in displacement and strain fields, respectively:

$$a_{u,i} = \left|\frac{u_i^{num} - u_i^{exact}}{u_i^{exact}}\right|, \text{ and } a_{e,i} = \left|\frac{\epsilon_i^{num} - \epsilon_i^{exact}}{\epsilon_i^{exact}}\right| \tag{21}$$

where ϵ_i^{num} and ϵ_i^{exact} the numerical and analytical strain at particle i, respectively. The L_2 norm and amplitude is set to be zero if the analytical solution is zero.

The old peridynamic scheme without any control of zero-energy modes (No control), two control methods adding artificial force states by linear springs (Springs) and average displacement

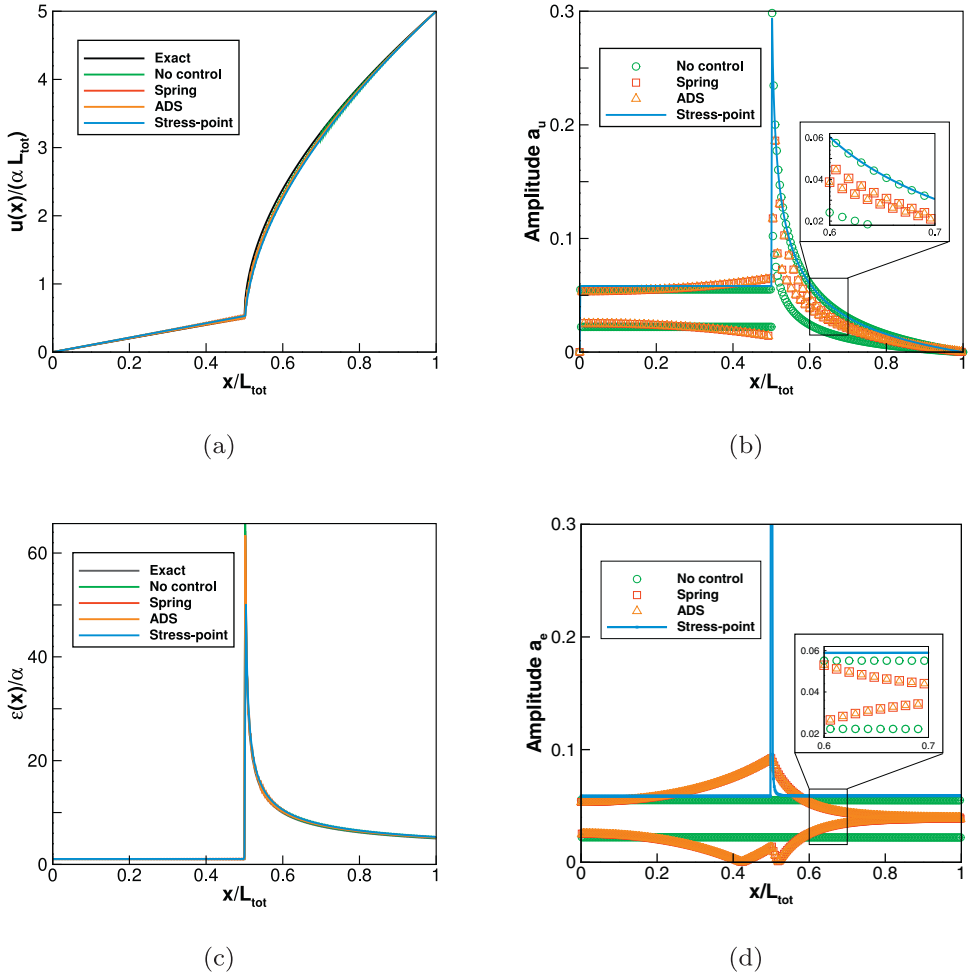

Fig. 7. Effect of zero-energy modes on displacement and strain fields of 1D bar based on four control methods. (a) and (c) are the displacement and strain distribution, respectively, while (b) and (d) are corresponding local amplitudes. Local zoomed-in views are provided to distinguish symbols. All Results are based on a mesh with 500 particles.

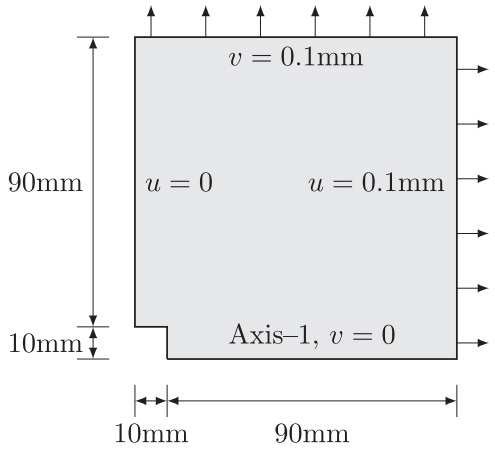

Fig. 8. A quarter of 2D elastic plate with a squared opening under uniform stretch. Symmetric displacement boundary conditions are applied at the border.

force states (ADS), and the new stress-point approach (Stress-point) are applied to solve the 1D numerical problem, respectively. Another penalty approach, which is the third control method in Breitenfeld et al. (2014); Yaghoobi and Chorzepa (2017), is not discussed, since it is conceptually similar to the method of applying supplemental forces along each bond. Four different mesh sizes are employed. Optimum values of C_1 and C_2 are obtained by multiple attempts beforehand, as elaborated in Breitenfeld et al. (2014); Yaghoobi and Chorzepa (2017). These values change with the mesh size and are listed in Table 1.

Table 1
Optimum values of C_1 and C_2 in (7) and (8) for adding artificial springs and average displacement states. n is the number of particles.

n	100	200	500	1000
C_1[a]	0.8	1.28	2	3
C_2[a]	60	150	500	1750

[a] C_1 and C_2 are not dimensionless.

Numerical results of the displacement and strain distribution, as well as their relative amplitudes of oscillation are plotted in Fig. 7. All results are based on a mesh size with 500 peridynamic particles. Even though all numerical results are close to the analytical results, as shown in Fig. 7(a) and (c), zero-energy modes are not alleviated in any method other than stress-point approach. In the amplitude plots, only stress-point approach has a smooth single line. Two or more separate lines are observed in other control methods and this is because the numerical solutions are oscillating between a range, the oscillations are not shown to improve plot clarity.

We find that adding force states can indeed suppress oscillations in the nonlinear region, i.e., $L_{tot}/2 < x \leq L_{tot}$, however, it fails in the linear region, $L_{tot}/2 < x \leq L_{tot}$. Another disadvantage of adding artificial force states, as we mentioned previously, is that their constants, C_1 and C_2, are supposed to be carefully selected before satisfactory results are obtained. Even worse, their optimum values are changing with mesh sizes, as shown in Table 1. Hence, in higher-dimensional examples we will be only be focused on comparisons between the stress-point model and the peridynamic model with no control of zero-energy modes. The stress-point method is demonstrated to be effective on suppressing zero-energy

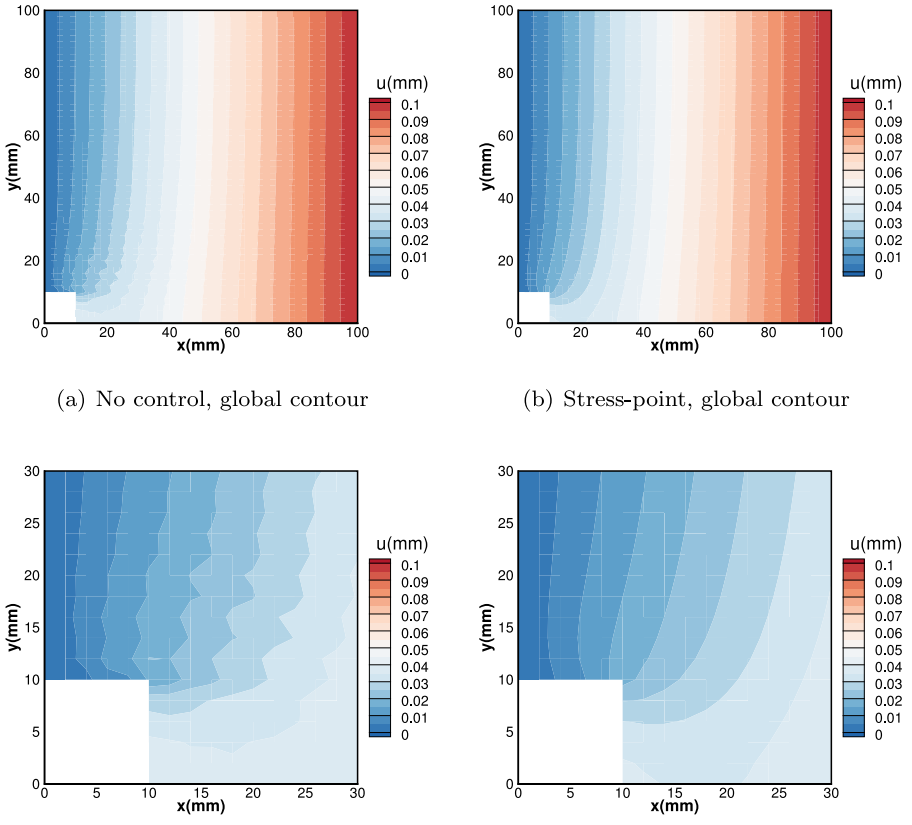

(a) No control, global contour

(b) Stress-point, global contour

(c) No control, zoomed-in opening

(d) Stress-point, zoomed-in opening

Fig. 9. Contours of the u-displacement obtained from the peridynamic model with no control of zero-energy modes and the new stress-point approach.

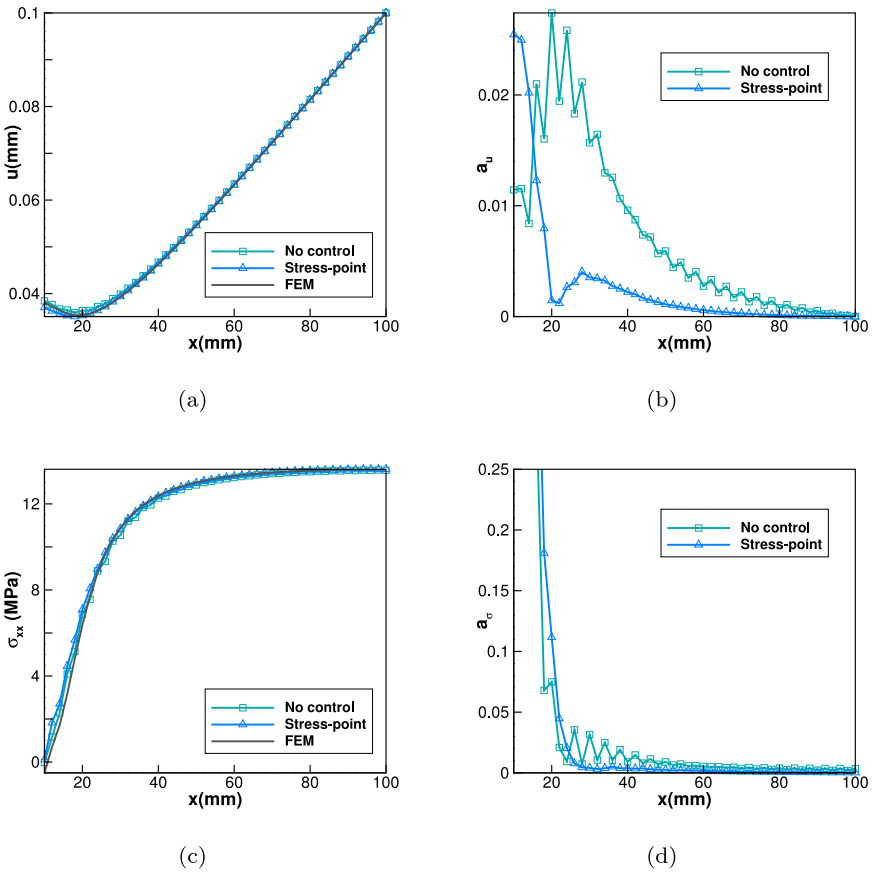

Fig. 10. Distributions of u-displacement, stress σ_{xx}, and their relative amplitudes along the axis-1 obtained from the peridynamic model with no control of zero-energy modes (No control), the new stress-point approach (Stress-point), and finite-element method (FEM).

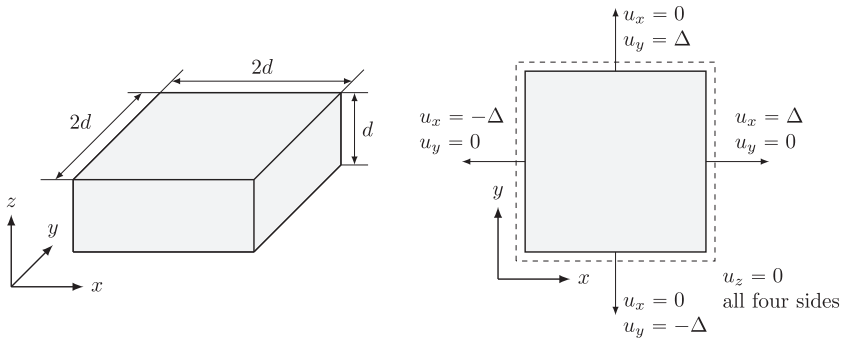

Fig. 11. A 3D elastic brick example with dimension $d = 40$ mm. Displacement boundary conditions are applied on four sides while the top and bottom are left traction-free. The small displacement increment is $\Delta = 0.4$ mm.

modes in the 1D bar example. Note that higher jumps are observed in Fig. 7(b) and (d) compared to analytical solution. This is because we average the stress based on stress-point values on the two sides at the point of discontinuity.

5.2. 2D plate test

An example of 2D elastic plate with a square hole at center under uniform stretch is modelled. We only consider a quarter of the plate due to symmetry with dimensions shown in Fig. 8. Displacement loading is applied at the four borders. The material is assumed to be isotropic elastic with Young's modulus $E = 1000$ MPa and Poisson's ratio $\nu = 0.3$. As seen here, compared to the variable Young's modulus $E(x)$ in the previous 1D example, a constant E can still bring in zero-energy modes in higher-dimensional problems.

Fig. 9 is a comparison of u-displacement contours based on the peridynamic model without any control of zero-energy modes (No control) and the stress-point approach (Stress-point, see Section 3.2). The particle spacing is $h = 2$ mm. Conspicuous oscillations can be observed around the squared opening in the results with no control of zero-energy modes, in contrast with smooth results using the stress-point method.

Next, we defined two local amplitudes of oscillation, $a_{u,\,i}$ and $a_{\sigma,\,i}$, at particle i to quantitatively measure the effect of zero-energy modes in the displacement and stress fields, respectively:

$$a_{u,i} = \left|\frac{u_i^{\mathrm{PD}} - u_i^{\mathrm{FEM}}}{u_i^{\mathrm{FEM}}}\right|, \text{ and } a_{\sigma,i} = \left|\frac{(\sigma_{xx})_i^{\mathrm{PD}} - (\sigma_{xx})_i^{\mathrm{FEM}}}{(\sigma_{xx})_i^{\mathrm{FEM}}}\right| \tag{22}$$

where superscripts PD and FEM denote the peridynamic and finite-element analysis results, respectively. We applied a quasi-static

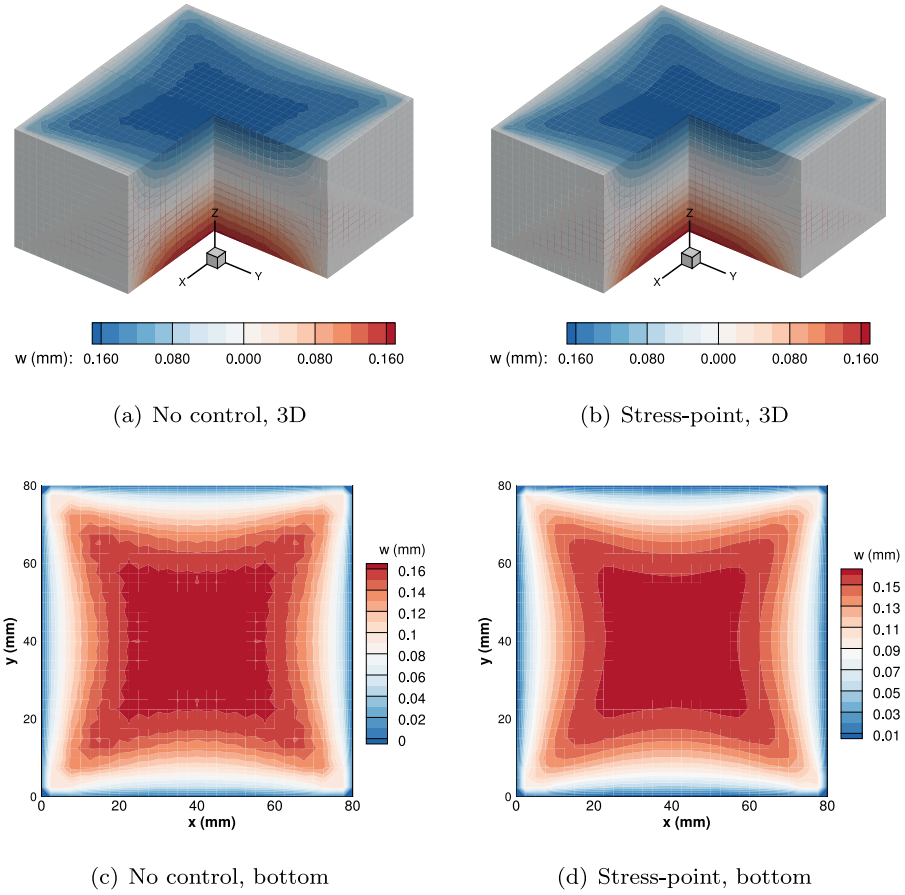

(a) No control, 3D (b) Stress-point, 3D

(c) No control, bottom (d) Stress-point, bottom

Fig. 12. Contours of z-displacement obtained from the peridynamic model with no control of zero-energy modes and the new stress-point approach. (a) and (b) are 3D contours while (c) and (d) are 2D contours of the bottom surface.

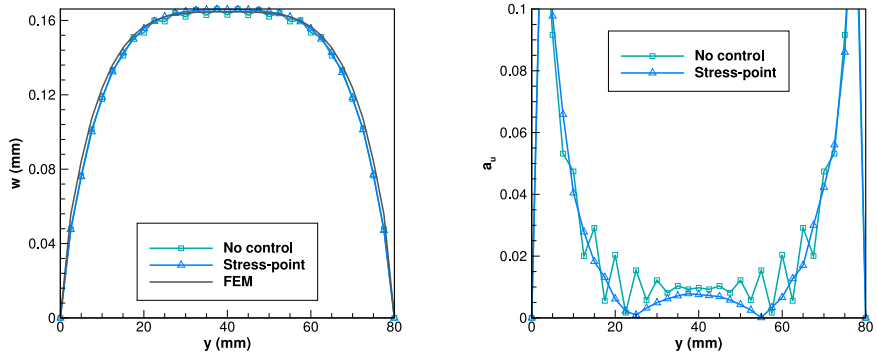

Fig. 13. Contours of z-displacement on a selected line located at $x = 40$ mm and $z = 0$ mm varied along y-direction. The peridynamic model with no control of zero-energy modes, the new stress-point approach, and finite-element method (FEM) are applied, respectively.

FEM formulation using four noded quadrilateral elements in the 2D problem and eight noded hexahedral elements in 3D. Finite-element nodes are assigned right at the place of peridynamic particles in order to quantitatively compare with peridynamic solutions with a vanishing horizon. Note that finite-element solutions (which are of local nature) are utilized as a reference rather than benchmark when we compare peridynamic results between the stress-point and no-control approaches.

The u-displacement, horizontal stress σ_{xx}, and their amplitudes of oscillations along the horizontal axis–1 ($y = 0$ mm, see Fig. 8) are plotted in Fig. 10. The disagreement between PD and FEM solutions mainly lies near the squared opening on the left. This is because PD is based on a non-local integral formulation wherein stress singularity at the sharp corner is avoided (Bower, 2009). If we pay closer attention to the region away from the left corner, i.e., $x > 20$ mm, the stress-point approach produces very smooth results, in both displacement and stress field, compared to oscillations in the old PD model without control of zero-energy modes.

5.3. 3D brick test

A 3D elastic brick example is considered in this section. The length-width-height ratio of the brick is $2d$: $2d$: d, where $d = 40$ mm. Displacement loadings are applied on its four sides, as shown in Fig. 11, while the top and bottom faces are left traction-free. The material is assumed isotropic with Young's modulus $E = 1000$ MPa and Poisson's ratio $\nu = 0.3$. The particle spacing is selected as $h = d/16 = 2.5$ mm.

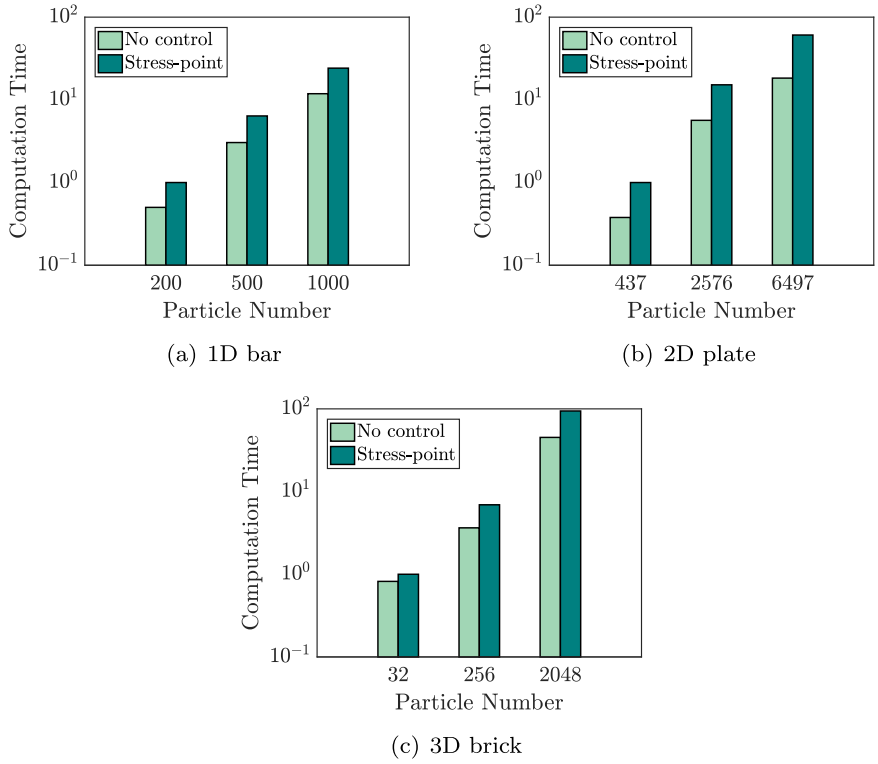

(a) 1D bar (b) 2D plate (c) 3D brick

Fig. 14. Performance tests between the peridynamic model with no control of zero-energy modes and the stress-point approach. The computation time is normalized by the stress-point case with least particle numbers in each test.

A comparison of z-displacement contours, computed by the old peridynamic model without any control of zero-energy modes (No control) and the stress-point approach (Stress-point), are plotted in Fig. 12. The overall contours are similar while disagreements exist. Serrated contours are observed if no control method is applied. Moreover, zero-energy modes are eliminated not only on the surface but also inside the brick, as shown in Fig. 12(b).

Next, we recomputed the 3D brick problem with the finite-element method and assigned element nodes right at the location of the peridynamic particles. The z-displacement and its relative amplitudes a_w, defined similar to (22) but based on z-displacement, on a selected line located at $x = 40$ mm and $z = 0$ mm varied along y-direction are shown in Fig. 13. The overall contours of the three methods are similar. Disagreements between peridynamics and finite-element method solutions come up near the boundaries due to the non-local integral formulation. As we move away from the boundary, zero-energy modes are more evident if no control method is applied. By contrast, the stress-point approach has a strong suppression effect on the oscillations.

5.4. Numerical efficiency test

Finally, a computation efficiency test on the new stress-point peridynamic model is conducted. We performed computational speed tests on three numerical examples including the 1D bar in Section 5.1, the 2D plate in Section 5.2, and the 3D brick in Section 5.3. Parallel computation was disabled and examples are run in serial on a single processor. Three different number of particles are employed in each example and the convergence criteria are the same with (17) as $e_l = 10^{-6}$. Results are shown in Fig. 14. Theoretically, the stress-point approach will take double the time compared to the old scheme because a smaller (halved) time step needed to strictly satisfy the stability condition (see Section 3.1). Furthermore, the stress-point peridynamic model has to compute more stress terms in one horizon based on the number of stress points. However, this higher computation cost is balanced by the ability to fully control zero-energy modes.

6. Conclusions and future work

A stress-point approach is proposed for the non-ordinary state-based peridynamic correspondence model to fully control zero-energy modes in a nearest neightbor model. We show that by computing two deformation gradients for each particle via splitting its neighborhood, zero-energy-mode oscillations in solutions can be completely damped. The method is first demonstrated in a simple 1D problem and then applied to 2D and 3D examples. In the 1D example, the stress-point approach is compared with analytical solutions and with finite element approach in higher dimensions. The method is demonstrated to be superior to other control methods with introduced supplementary force states. Future work will include extension of this approach to larger horizon sizes and nonlinear problems involving plasticity.

Acknowledgments

The computations have been carried out as part of research supported by the U.S. Department of Energy, Office of Basic Energy Sciences, Division of Materials Sciences and Engineering under Award no. DE-SC0008637 that funds the PRedictive Integrated Structural Materials Science (PRISMS) Center at the University of Michigan.

Appendix A. Stability analysis on 1D elastic problems with nearest-particle discretizations

Typically, wave motions in solid mechanics are modeled by hyperbolic partial differential equations (Bower, 2009; LeVeque, 2007). Assume a 1D bar is elastic under small deformation, and

ignore the body force and damping ratio, the equation of motion can be expressed by displacement u as

$$\frac{\partial^2 u}{\partial t^2} = \frac{1}{\rho}\frac{\partial \sigma}{\partial x} = c_s^2 \frac{\partial^2 u}{\partial x^2}, \tag{A.1}$$

where $c_s = \sqrt{E/\rho}$ is the speed of sound, E and ρ are the Young's modulus and density, respectively.

In a discrete system with totally N particles, let u_j^n indicate the displacement component of particle j at time $t = n\Delta t$, where Δt is the time step assumed constant, and $\mathbf{u}^n = [u_1^n, u_2^n, \ldots, u_N^n]$ be the displacement vector at $t = n\Delta t$. With a central difference discretization at time and a peridynamic discrete operator $\mathcal{A}$ at space, (A.1) turns into

$$\frac{\mathbf{u}^{n+1} - 2\mathbf{u}^n + \mathbf{u}^{n-1}}{(\Delta t)^2} = \mathcal{A}(\mathbf{u}^n). \tag{A.2}$$

A1. The peridynamic scheme with no control of zero-energy modes

Based on a discretization scheme in Luo et al. (2017), without any treatment of zero-energy modes, the peridynamic operator can be rewritten as an explicit matrix form, i.e., $\mathcal{A}(\mathbf{u}^n) = \mathbf{A}_1\mathbf{u}^n$, with

$$\mathbf{A}_1 = \frac{c_s^2}{4(\Delta x)^2}\begin{bmatrix} \cdots & & & & \cdots & & & \cdots \\ \cdots & 1 & 0 & -2 & 0 & 1 & & \cdots \\ \cdots & & 1 & 0 & -2 & 0 & 1 & \cdots \\ \cdots & & & 1 & 0 & -2 & 0 & 1 & \cdots \\ \cdots & & & & \cdots & & & \cdots \end{bmatrix}. \tag{A.3}$$

It becomes a standard initial value problem for hyperbolic systems. Modified equations analysis is an approach to reveal stability behavior of the numerical solution (LeVeque, 2007). The main idea of modified equations analysis is to find another partial differential equation which is approximated by the current discretization scheme. By doing Taylor series expansions, the modified equation of (A.2) is calculated as

$$\frac{\partial^2 u}{\partial t^2} - c_s^2\frac{\partial^2 u}{\partial x^2} = -\frac{1}{12}c_s^2(\Delta x)^2\left[\mu_c^2 - 4\right]\frac{\partial^4 u}{\partial x^4} + \cdots \tag{A.4}$$

where $\mu_c = c_s\frac{\Delta t}{\Delta x}$ is the CFL number. (A.4) is the partial differential equation better approximated by the peridynamic scheme (A.3). The derivative terms on the right hand side are not in the original partial differential equation and constitute truncation error introduced by finite-differencing. As the mesh is refined, these terms will become smaller and smaller and we end up solving the original differential equation. The order of accuracy of a finite-difference scheme is defined by the lowest-order powers of the increments Δt and Δx appearing in the fourth order terms of the modified equation. Based on the right side of (A.4), we have a second order accurate scheme for (A.1).

The necessary condition for stability is obtained from Von Neumann analysis (Warming and Hyett, 1974). The important result is that the necessary condition for stability depends on the sign of the coefficient of the lowest even-order derivative on the right hand side. The stability condition is thus,

$$\mu_c^2 - 4 \le 0 \Longrightarrow \Delta t \le 2\Delta x/c_s. \tag{A.5}$$

Therefore, the critical time step for 1D elastic problems is $\Delta t_c = 2\Delta x/c_s$.

The structure of matrix $\mathbf{A}_1$ in (A.3) shows a weak coupling between neighbor particles, as five particles are involved in one equation while roles of the second and fourth particles are missing.

A2. The new peridynamic scheme with stress-point approach

Assume the material is elastic and under small deformation, stresses in (11) are calculated as

$$\sigma_{1,r} = E_1\epsilon_{1,r} = E_1\frac{u_2 - u_1}{L}, \quad \sigma_{2,l} = E_2\epsilon_{2,l} = E_2\frac{u_2 - u_1}{L},$$
$$\sigma_{2,r} = E_2\epsilon_{2,r} = E_2\frac{u_3 - u_2}{L}, \quad \sigma_{3,l} = E_3\epsilon_{3,l} = E_3\frac{u_3 - u_2}{L}. \tag{A.6}$$

Based on (11) and (A.6), the peridynamic space operator in (A.2) can be expressed as a new explicit matrix production, i.e., $\mathcal{A}(\mathbf{u}^n) = \mathbf{A}_2\mathbf{u}^n$, with

$$\mathbf{A}_2 = \frac{c_s^2}{(\Delta x)^2}\begin{bmatrix} \cdots & & & \cdots & & \cdots \\ \cdots & 1 & -2 & 1 & & \cdots \\ \cdots & & 1 & -2 & 1 & \cdots \\ \cdots & & & 1 & -2 & 1 & \cdots \\ \cdots & & & \cdots & & \cdots \end{bmatrix}, \tag{A.7}$$

which is more compact than $\mathbf{A}_1$ in (A.3). The modified equation for the new scheme becomes

$$\frac{\partial^2 u}{\partial t^2} - c_s^2\frac{\partial^2 u}{\partial x^2} = -\frac{1}{12}c_s^2(\Delta x)^2\left[\mu_c^2 - 1\right]\frac{\partial^4 u}{\partial x^4} + \cdots \tag{A.8}$$

Although the equation above is structurally similar to (A.4), the necessary stability condition is different due to the differences in the leading coefficients in the fourth order term. The stress point method has the stability condition:

$$\mu_c^2 - 1 \le 0 \Longrightarrow \Delta t \le \Delta x/c_s. \tag{A.9}$$

Hence, the critical time step is reduced to a half of the old scheme. Note that this analysis is restricted to the nearest neighbor discretization used in this work. As shown in Silling and Askari (2005), the maximum stable time step for peridynamics is, in general, also a function of the peridynamic horizon for higher order interactions.

References

Agwai, A., Guven, I., Madenci, E., 2011. Predicting crack propagation with peridynamics: a comparative study. Int. J. Fract. 171 (1), 65–78.

Bažant, Z.P., Belytschko, T.B., Chang, T., 1984. Continuum theory for strain–softening. J. Eng. Mech. 110 (12), 1666–1692.

Bower, A.F., 2009. Applied Mechanics of Solids. CRC Press.

Breitenfeld, M.S., Geubelle, P.H., Weckner, O., Silling, S.A., 2014. Non-ordinary state-based peridynamic analysis of stationary crack problems. Comput. Methods Appl. Mech. Eng. 272, 233–250.

Coleman, B.D., Hodgdon, M.L., 1985. On shear bands in ductile materials. Arch. Ration. Mech. Anal. 90 (3), 219–247.

Dyka, C.T., Randles, P.W., Ingel, R.P., 1997. Stress points for tension instability in SPH. Int. J. Numer. Methods Eng. 40 (13), 2325–2341.

Flanagan, D.P., Belytschko, T., 1981. A uniform strain hexahedron and quadrilateral with orthogonal hourglass control. Int. J. Numer. Methods Eng. 17 (5), 679–706.

Ganzenmüller, G.C., Hiermaier, S., May, M., 2015. On the similarity of meshless discretizations of peridynamics and smooth-particle hydrodynamics. Comput. Struct. 150, 71–78.

Gerstle, W.H., 2015. Introduction to Practical Peridynamics: Computational Solid Mechanics Without Stress and Strain, 1. World Scientific Publishing Co Inc.

Ghosh, S., Kumar, A., Sundararaghavan, V., Waas, A.M., 2013. Non-local modeling of epoxy using an atomistically-informed kernel. Int. J. Solids Struct. 50 (19), 2837–2845.

Ghosh, S., Sundararaghavan, V., Waas, A.M., 2014. Construction of multi-dimensional isotropic kernels for nonlocal elasticity based on phonon dispersion data. Int. J. Solids Struct. 51 (2), 392–401.

Kilic, B., Madenci, E., 2010. An adaptive dynamic relaxation method for quasi-static simulations using the peridynamic theory. Theor. Appl. Fract. Mech. 53 (3), 194–204.

LeVeque, R.J., 2007. Finite Difference Methods for Ordinary and Partial Differential Equations: Steady-state and Time-dependent Problems. SIAM.

Littlewood, D.J., 2011. A nonlocal approach to modeling crack nucleation in AA 7075-t651. In: ASME 2011 International Mechanical Engineering Congress and Exposition. American Society of Mechanical Engineers, pp. 567–576.

Luo, J., Ramazani, A., Sundararaghavan, V., 2017. Simulation of micro–scale shear bands using peridynamics with an adaptive dynamic relaxation method. Int. J. Solids Struct..

Madenci, E., Barut, A., Futch, M., 2016. Peridynamic differential operator and its applications. Comput. Methods Appl. Mech. Eng. 304, 408–451.

Madenci, E., Oterkus, E., 2014. Peridynamic Theory and its Applications, 17. Springer.
Silling, S.A., 2000. Reformulation of elasticity theory for discontinuities and long-range forces. J. Mech. Phys Solids 48 (1), 175–209.
Silling, S.A., 2017. Stability of peridynamic correspondence material models and their particle discretizations. Comput. Methods Appl. Mech. Eng. 322, 42–57.
Silling, S.A., Askari, E., 2005. A meshfree method based on the peridynamic model of solid mechanics. Comput. Struct. 83 (17–18), 1526–1535.
Silling, S.A., Epton, M., Weckner, O., Xu, J., Askari, E., 2007. Peridynamic states and constitutive modeling. J. Elast. 88 (2), 151–184.
Sun, S., Sundararaghavan, V., 2014. A peridynamic implementation of crystal plasticity. Int. J. Solids Struct. 51 (19), 3350–3360.
Sundararaghavan, V., Waas, A., 2011. Non-local continuum modeling of carbon nanotubes: physical interpretation of non-local kernels using atomistic simulations. J. Mech. Phys. Solids 59 (6), 1191–1203.
Tupek, M.R., Radovitzky, R., 2014. An extended constitutive correspondence formulation of peridynamics based on nonlinear bond-strain measures. J. Mech. Phys. Solids 65, 82–92.
Vignjevi, R., Campbell, J., Libersky, L., 2000. A treatment of zero-energy modes in the smoothed particle hydrodynamics method. Comput. Methods Appl. Mech. Eng. 184 (1), 67–85.
Warming, R., Hyett, B., 1974. The modified equation approach to the stability and accuracy analysis of finite-difference methods. J. Comput. Phys. 14 (2), 159–179.
Wu, C.T., Ben, B., 2015. A stabilized non-ordinary state-based peridynamics for the nonlocal ductile material failure analysis in metal machining process. Comput. Methods Appl. Mech. Eng. 291, 197–215.
Yaghoobi, A., Chorzepa, M.G., 2017. Higher–order approximation to suppress the zero-energy mode in non-ordinary state-based peridynamics. Comput. Struct. 188, 63–79.